Shielding Electrostatic Fields in Polar Semiconductor Nanostructures

G. M. O. Hönig,[1,2,*] S. Westerkamp,[1] A. Hoffmann,[1] and G. Callsen[1,†]

[1]Institut für Festkörperphysik, Technische Universität Berlin, Hardenbergstrasse 36, 10623 Berlin, Germany

[2]Bundesanstalt für Materialforschung und -prüfung (BAM), Unter den Eichen 87, 12205 Berlin, Germany

(Received 25 April 2016; revised manuscript received 8 November 2016; published 6 February 2017)

Polar semiconductor materials enable a variety of classic and quantum-light sources, which are optimized continuously. However, one key problem—the inherent electric crystal polarization of such materials—remains unsolved and deteriorates the radiative exciton decay rate. We suggest a sequence of reverse interfaces to compensate these polarization effects, while the polar, natural crystal growth direction is maintained. Former research approaches, like growth on less-polar crystal planes or even the stabilization of unnatural phases, never reached industrial maturity. In contrast, our concept provides a way for the development of ultrafast devices based on established growth processes for polar materials, while the electric potential landscape becomes adjustable.

DOI: 10.1103/PhysRevApplied.7.024004

I. INTRODUCTION

Nowadays, visible and ultraviolet light generation mainly relies on wurtzite, group-III nitride nanostructures that enable not only classic emitters [light-emitting diodes (LEDs) or laser diodes (LDs)] but a variety of quantum-light sources [1]. The advantages of this polar material system, like robustness, brilliance, and integratability, come at the cost of a piezo- and pyroelectric polarization along the natural [0001] growth direction [2], altogether creating huge electrostatic fields (MV/cm) across the optically active regions [3]. Hence, any beneficial exciton confinement in related nanostructures is always counterbalanced by a field-induced, spatial electron-hole separation spoiling the light generation in the active region [4].

Here, we demonstrate that our internal-field-guarded active-region design (IFGARD) [5] can lock the polarization fields out of any active region in polar heterostructures, yielding a boost in the radiative exciton decay rate by orders of magnitude. Previous attempts to tackle the polarization fields did not achieve any pronounced relevance. Stabilizing the cubic phase of nitrides [6] deteriorates the crystal quality [7,8], turning the bright nitrides into rather dim emitters [9]. Similarly, the realization of alternative growth directions can (partially) avoid the polarization fields but again suffers from a strongly reduced crystal quality besides additional technological challenges [10]. In contrast, the IFGARD bears on decades of research that was dedicated to improve the quality of strongly polar materials based on their most natural growth direction [11,12]. Hence, our approach combines two advantages: well-established, high-quality, polar material growth and augmented exciton decay rates. Generally, the IFGARD can not only serve classical applications as LEDs and LDs, but it breaks ground for efficient and ultrafast quantum-light sources based on (individual) quantum dots (QDs).

II. FIELD GUARDING IN QDs

Commonly, the emissive active region of devices features a smaller band gap than the matrix material in its surroundings, providing the beneficial carrier-confinement effect; cf. Fig. 1(a). In terms of light reabsorption, it appears as a ludicrous approach to encapsulate this sandwich by the active-region material as shown in Fig. 1(d). In this counterintuitive design, a significant fraction of the emitted light gets reabsorbed by the so-called guard layers. However, guard material thicknesses below the emitted wavelength absorb only a well-tolerable amount of emitted photons, as discussed in Appendix A—an effect that is overcompensated by the advantages of the IFGARD.

In order to exemplify the IFGARD, we first choose a GaN QD embedded in AlN—a selection that does not restrict the general applicability of the entire concept to a specific material system [polar materials like, e.g., ZnO/(Zn, Mg)O, [111]-(In, Ga)As/GaAs, and GaN/(Al, Ga)N] or nanostructure (QD, nanowire, quantum well, etc.). Figure 1 summarizes the major differences between a conventional GaN QD and its IFGARD counterpart in the first and second row, respectively focusing from left to right on the composition, the polarization fields, and the band structure. Here, the horizontal c axis denotes the most favorable, natural [0001] growth direction of III-nitrides. Figure 1(a) shows a GaN QD with a height (horizontal) of 2 nm (dark gray) embedded in a matrix of AlN (light gray), while the IFGARD equivalent features thin AlN barriers and additional GaN guard layers, as depicted in Fig. 1(d). A significant interface charge buildup occurs at the

*Gerald.Hoenig@physik.tu-berlin.de
†Gordon.Callsen@physik.tu-berlin.de

 © 2017 American Physical Society

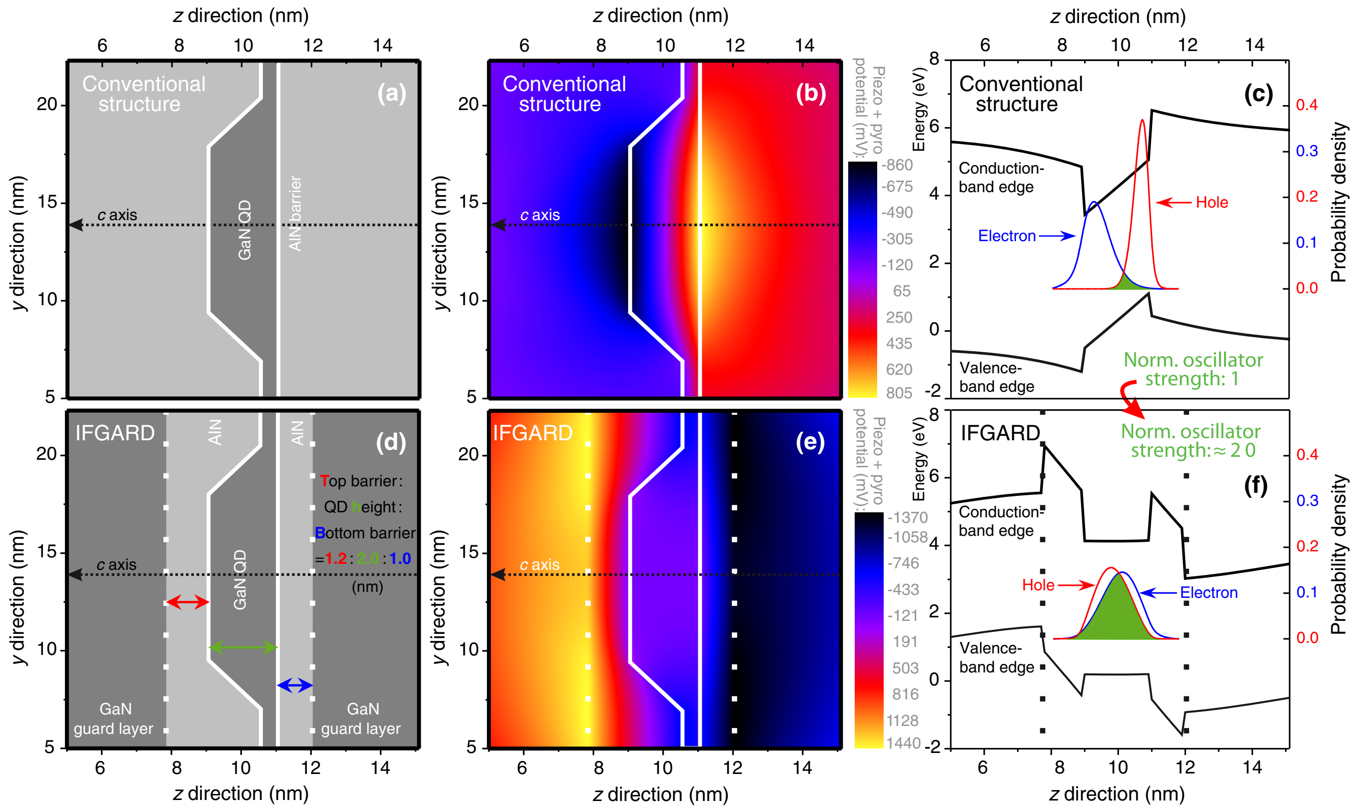

FIG. 1. Comparison between a conventional QD structure (first row) and a QD comprising the IFGARD (second row). From left to right: The particular layer sequence is illustrated for the GaN/AlN case in the 2D scans in (a) and (d). The contour plots in (b) and (e) show the sum of the piezo- and pyroelectric potential for the conventional and the IFGARD QD structure. Consequently, the band-edge scans (c) and (f) through the QD center along the c axis exhibit a prominent tilt [(b), yellow → black gradient] inside the conventional QD (c), while the IFGARD QD features a constant potential (f), as evidenced by the constant, central, purple coloring in (e). Consequently, the potential gradient inside the conventional QD structure separates the charge carriers, as shown by the electron (blue) and hole (red) probability density in (c). In contrast, a drastically increased electron-hole overlap is obtained for the IFGARD QD (f), causing a beneficial boost in the exciton recombination rate.

AlN-GaN-AlN interfaces, yielding a potential drop of approximately 1.7 V for the conventional case—right across the 2-nm-high QD as shown in the color-coded image of Fig. 1(b). The associated polarization potential overlays the band structure, provoking the band edges to be tilted, as shown in Fig. 1(c). As a result, not only a redshift of the emission wavelength occurs but also the electron and hole are spatially separated along the c axis, lowering their overlap and subsequently the exciton decay rate. Figure 1(c) illustrates this matter based on the electron (blue) and hole (red) probability density profiles along the c axis and the corresponding overlap (colored in green). The entire phenomenon that counteracts the confinement-induced blueshift of the QD emission is known as the quantum-confined Stark effect (QCSE) and has been studied in great profusion in the last decades [13–16]. It is exactly this QCSE that researchers sought to overcome, e.g., by stabilizing the cubic crystal structure phase or by realizing numerous alternative growth directions of III-nitrides.

Generally, the same charge buildup occurs for the IFGARD case in Fig. 1(d). However, due to the inclusion of the guard layers, the polarization potential gradient is now suspended from the QD. In other words, by adding two additional GaN-AlN interfaces as described by the IFGARD, one can suppress the electric field inside of the QD, as illustrated in Fig. 1(e). Here, the constant purple coloring of the QD approves constancy for the sum of the piezo- and pyroelectric polarization potential—the main benefit of the IFGARD. As a result, one obtains flat conduction- and valence-band edges within the QD, a strongly reduced charge-carrier separation along the c axis, and, as a direct consequence, an enhanced electron-hole overlap, as shown in Fig. 1(f). Therefore, in comparison to the conventional case, the IFGARD raises the directly related oscillator strength by a factor of 20 for the common QD dimensions assumed in Fig. 1. This improvement directly translates to a factor of 20 in the rate of emitted single photons from such a GaN QD. Please note that all information regarding the simulations (eight-band-$k \cdot p$ implementation [17]) and QD dimensions can be found in the Appendix B; cf. Fig. 5. Also, the electron-hole particle interaction is considered for the exciton (Hartree-Fock treatment).

III. TAILORING BUILT-IN FIELDS

The QD emission characteristic is dominated by the polarization effects inherent to the crystal lattice and not by the influence of strain on the band structure—in this context, an almost negligible [18–20] but, nevertheless, still considered effect (see Appendix B). Therefore, we focus on the electric potential instead of the band-edge profiles in order to illustrate the IFGARD effect in the following. Annihilating the QCSE by canceling out the electric fields generated by the interface charges positioned on the opposite sides of the QD and barriers always exhibits the most tremendous effect. However, some fine-tuning of the AlN barrier thicknesses is needed in order to reach a fully optimized field cancellation for QDs not only due to their top and bottom facets of different size but also due to their inclined side facets. Please note that these *top* and *bottom* facets match the *left* and *right* GaN-AlN interface of the QD in Fig. 1, in agreement with Fig. 2, in order to allow a convenient comparison.

Figure 2 focuses on the influence of structural IFGARD parameters on the polarization potential within another, here, 3-nm-high (h) QD—to show the general applicability of the IFGARD concept, independent of the QD dimensions. By varying the top AlN barrier thickness (t, red) above and the bottom barrier thickness (b, blue) below the QD [compare Fig. 1(d)], the gradient of the built-in electric potential varies, as plotted in Fig. 2(a). By symmetrically decreasing both barrier widths ($t = b$), the potential gradient evolves from a drop (blue curve) within the QD for thick barriers (regarding a positive probe charge) to a corresponding rise for thinner barriers (red curve). AlN barrier thicknesses between 1.5 and 2.0 nm ($t = b$) yield the smallest slopes for the potential trends as long as symmetric barriers are considered. However, the potential drop inside of the QD can be reduced even further if different barrier thicknesses are considered ($t \neq b$). We find the combination of 1.5- and 2.0-nm-thick AlN barriers to be ideal for reducing the absolute potential drop from the top to the bottom edge of the 3-nm-high IFGARD QD down to 5 mV. Interestingly, the inversion of the stack sequence ($t \leftrightarrow b$) neither significantly alters the gradient nor the particular trend for the electric potential, as evidenced by the black and green curves in Fig. 2(a). Here, the bottom barrier thickness regulates only the absolute value of the potential inside of the QD in regard to the same arbitrarily chosen zero. As soon as the flat-potential conditions are approached, a potential bowing becomes apparent originating from the piezoelectric polarization caused by the particular strain distribution inside of the QD. It is of utmost importance to note that exactly the same 3-nm-high QD embedded in a conventional structure is affected by a total potential drop of -2112 mV as indicated in Fig. 2(a) (dashed, orange line) in contrast to the IFGARD optimum of -5 mV. Therefore, we use exactly this straightforwardly accessible total potential drop (PD) as a convenient measure for the degree of internal field guarding due to the IFGARD.

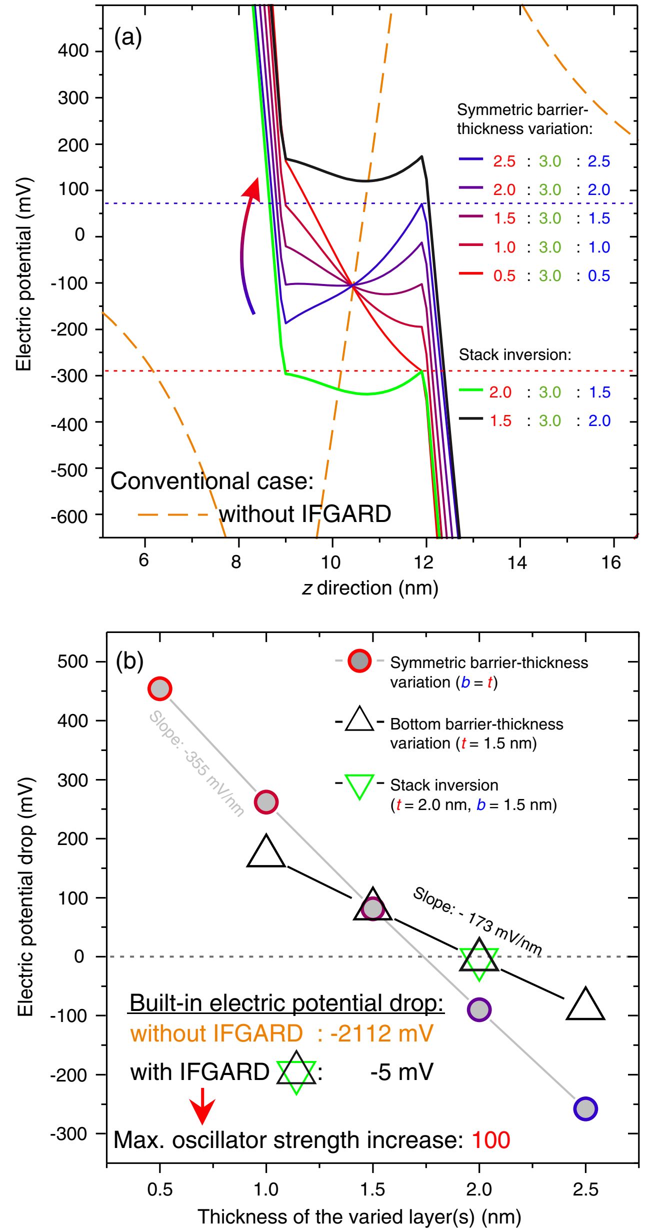

FIG. 2. (a) Piezo- and pyroelectric potential traces across a QD with a height of $h = 3$ nm are shown for different AlN barrier thicknesses t, b. A symmetric barrier-thickness variation ($t = b$) tunes the inclination of the potential gradients (blue → red), whereas a stack inversion with asymmetric barrier thicknesses ($t \neq b$) results only in a potential offset. The entire electric potential drop inside of the QD is evaluated in (b) for several barrier thicknesses, indicating the optimum configuration by a double triangle. Vanishing of the electric potential drop causes a 100-times-larger oscillator strength if compared to the conventional QD case.

Figure 2(b) plots PD values extracted from Fig. 2(a) following the applied color coding. We derive a slope of -355 mV/nm for the PD values corresponding to the symmetric ($t = b$) barrier-thickness increase [red to blue circles in Fig. 2(b)], whereas the sole increase of

b ($t = 1.5$ nm) yields a slope of -173 mV/nm [black triangles in Fig. 2(b)]—a direct pathway for future tuning attempts. The inversion of the IFGARD stack ($t \leftrightarrow b$) does not significantly alter the PD value, as indicated by the double triangle in Fig. 2(b) (green and black) and the potential scans in Fig. 2(a) that are colored accordingly. Figure 2(b) proves the fact that both negative and positive PD values are accessible by the presented concept, allowing the IFGARD to reach the desirable flat-band condition [compare Fig. 1(f)] under any reasonable operating voltage in case of electrically driven devices.

Barrier thickness constellations of $t = 2.0$ nm, $b = 1.5$ nm, or vice versa boost the oscillator strength by a factor of 100 if compared to the conventional 3-nm-high QD embedded in AlN. In other words, the photon rate provided by each of such GaN QDs is increased by 2 orders of magnitude. Nevertheless, the advantages of the IFGARD go beyond such a tremendous increase in overall QD brilliance. The absence of the QCSE for the IFGARD case in Fig. 1(d) leads to a QD emission energy of 4.2 eV, which is now exclusively governed by the confinement, whereas the conventional QD from Fig. 1(a) emits at 3.5 eV due to the QCSE redshift. In direct comparison to the 50% higher QD from Fig. 2 with emission energies of 2.9 and 4.0 eV, for the respective conventional and optimum IFGARD constellations, the QD size dependence of the emission energies is reduced by a factor of 3 from 3.5 eV–2.9 eV = 0.6 eV to 4.2 eV–4.0 eV = 0.2 eV. Hence, the energetically broad luminescence of conventional, e.g., nitride QD ensembles, is minimized by the IFGARD. This minimized luminescence broadness is a fundamental prerequisite for any laser application, e.g., with a QD gain medium, as the QD dimensions will predominantly affect their emission energy via the quantum confinement—a parameter of minor significance if compared to the QCSE in nitrides.

IV. FIELD GUARDING IN QUANTUM WELLS

After having exemplified the basic field-guarding concept and its adjustability for the case of QDs, we now come to an intuitive explanation regarding the functionality of the IFGARD based on the quantum-well (QW) structure exemplified in Fig. 3(a). Here in this figure, the GaN IFGARD QD from Fig. 1(d) is replaced by a GaN QW, again exhibiting a horizontally orientated c axis. Similar to the QD case in Fig. 1(e), interface charges build up at each of the GaN-AlN or AlN-GaN interfaces of the IFGARD QW structure, as illustrated in Fig. 3(a) by the + (red) or − (black) signs. Because of this particular reverse-interface sequence of the IFGARD, it is now feasible to achieve flat-band conditions inside of the single QW, as shown in Fig. 3(b) top (black line) for a 2-nm-thick single GaN QW encapsulated by two AlN barrier layers each with a thickness of $t = b = 1$ nm. In comparison, the conventional QW ($h = 2$ nm) illustrated by the red dotted line at the top of Fig. 3(b) exhibits a pronounced band-structure inclination.

Already the fundamental symmetry of this QW IFGARD structure brings an intuitive analogy to mind: a stack of

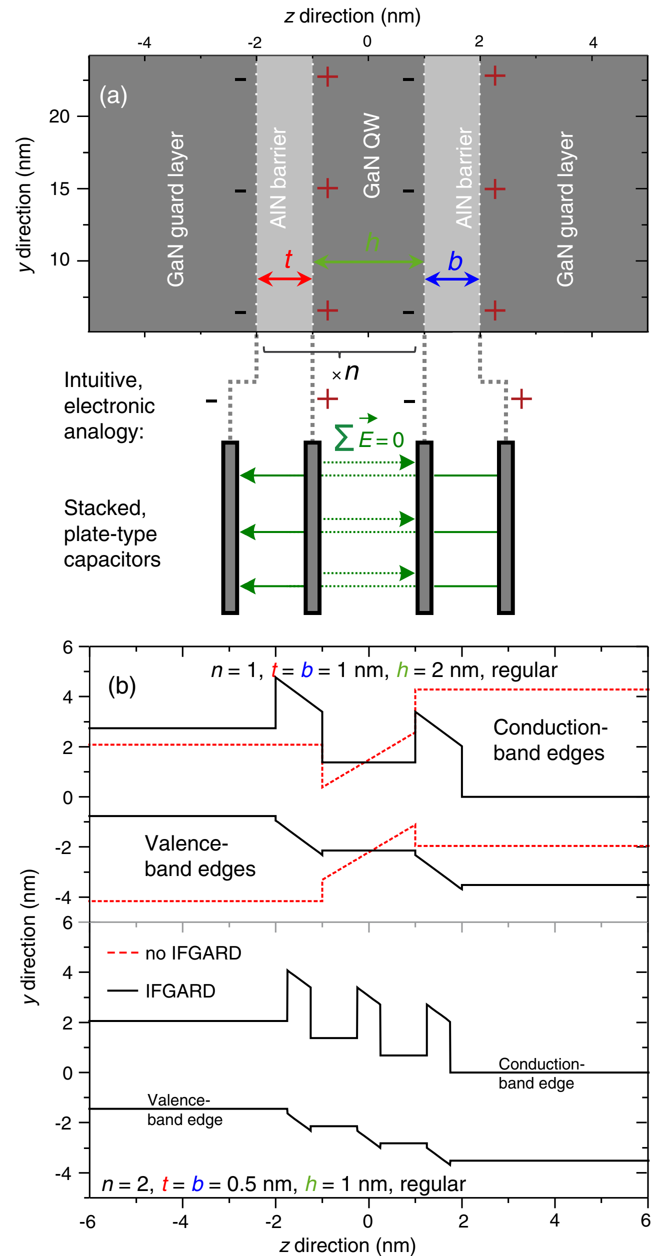

FIG. 3. The physics behind the field-guarding concept is explained based on its application to QWs, as illustrated in (a). Interface charges occur due to the crystal polarization (plus and minus signs), a situation similar to stacked open-circuit plate-type capacitors; cf. (a). Again, the polar crystal axis is horizontal, matching the scan direction for the band-edge profiles in (b). Neither the QW (h) nor the barrier thickness (t, b) have an influence on the flat-band condition within the individual QW. Even multiple (n) stacks of the fundamental IFGARD layer sequence are achievable, as exemplified for a regular double QW. Here, the barrier thickness exclusively governs the step height in the band structure. Please see Fig. 4 for a variation of the QW number, composition, and thickness.

open-circuit plate-type capacitors; cf. Fig. 3(a). In this analogy, the distance between the capacitor plates corresponds to the thicknesses of the GaN QW and the AlN barriers. The crystal's pyro- and piezoelectricity causes constant space-charge densities at the interfaces of the IFGARD heterostructure similar to a charged plate-type capacitor. Here, the central capacitor plates depicted in Fig. 3(a) generate an electric field that can exactly be neutralized by the reversed field caused by the outer capacitor plates resulting in a field-free zone similar to the field-guarded interior of the IFGARD QW structure. Generally, the homogeneous electric field between the capacitor plates remains constant if their distance is varied, and only the voltage ascribed to the potential difference between the charged surfaces changes. In analogy, changing the thickness of the GaN QW or AlN barriers does not spoil the field-guarding effect as the relevant electric field superposition inside of the QW remains zero. Exactly the same observation is true for the electric field across a particular AlN barrier, which is in our analogy evoked by the charged, left *or* right plates of the inner *and* outer plate-type capacitor. Such a constant nonzero electric field inside each of the AlN barriers is directly evidenced by a potential drop over a certain length interval in the corresponding band-structure calculations shown in Fig. 3(b). A constant slope of the band-structure trend (equivalent to constant electric fields) inside (nonzero) or outside (zero) the AlN barriers is caused by the fixed space charges at all GaN-AlN and AlN-GaN interfaces evoked by pyro- and piezoelectricity. Interestingly, the analogy of stacked open-circuit plate-type capacitors facilitates a most simplistic understanding of QW IFGARD heterostructures as long as plan-parallel interfaces of infinite size are assumed.

The analogy gets into difficulties for the QD case as interfaces of different size occur in addition to less-polar QD side facets. Hence, a more-complex nanostructure always requires the applied numerical 3D solution for the field situation detailed in Appendix B. However, it is exactly the deviating interface geometry in the IFGARD QD structures that allows the tuning of the field inside of the QD by barrier-thickness variations; cf. Fig. 2. Generally, the fundamental IFGARD stack comprises exactly one barrier (e.g., AlN) along with one QW [e.g., GaN; see Fig. 3(a)] and can arbitrarily be repeated (counted by $n \in \mathbb{N}$) without sacrificing the beneficial IFGARD effect seen, e.g., in the bottom of Fig. 3(b) for a 1-nm-thick double QW. By repeating the IFGARD stack, one can create a stepwise multi-QW structure exhibiting flat-band conditions within each QW. Such IFGARD QW stacking is neither limited by the number of QWs nor by the particular QW or barrier thickness, as shown in Figs. 4(a)–4(c). By repeating the IFGARD stack, one can create a stepwise multi-QW structure exhibiting flat-band conditions within each QW. Here, the barrier thickness just regulates the height of each potential step. It is important to understand that any IFGARD stacking is not restricted to QW structures and can also be applied to any other type of nanostructure. Even more-complex IFGARD band-structure schemes become accessible as soon as the

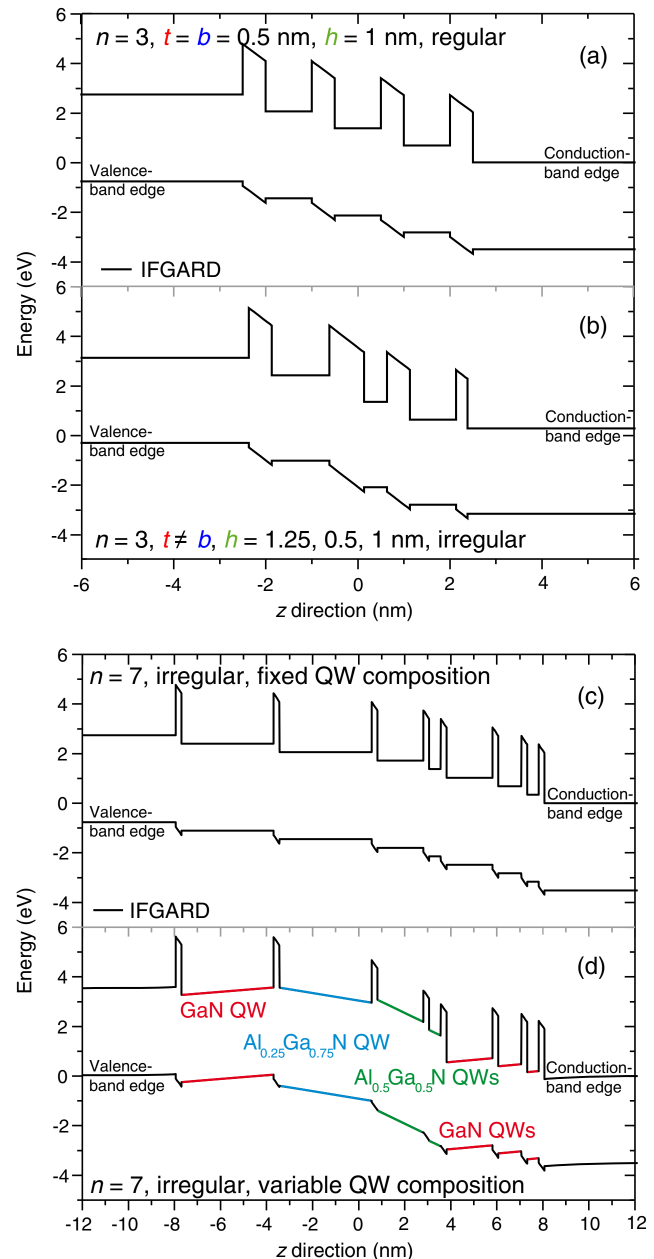

FIG. 4. (a)–(c) The electric field guarding effect is maintained even for extended stacks of QWs—here, three or up to seven are chosen arbitrarily—as the flat-band conditions in the active region are still preserved, while the barrier thickness tunes only the step height between neighboring QWs. (d) Any composition variation in the QWs leads to a direct adaptability of the immanent band-structure inclination and step height. As a result, positive and negative band-structure tilts become accessible independent of the individual QW thickness, governed only by the particular $(Al_{1-x}Ga_x)N$ composition. For simplicity, we choose an AlN barrier thickness of 0.25 nm in (c),(d) to approximate the thinnest possible structure of one monolayer.

active-region material composition is altered (e.g., within the $(\mathrm{Al}_{1-x},\mathrm{Ga}_x)\mathrm{N}$ system) in regard to the guard layers, as discussed in Appendix C. As a result, highly unconventional and formerly inaccessible potential landscapes can be generated, as outlined in Fig. 4.

V. DISCUSSION

Generally, the particular layer sequence of any IFGARD nanostructure can be realized straightforwardly based on well-established technologies that can even approach the deposition of single monolayers of material; cf. Appendix D. As a result, numerous IFGARD advantages come into reach at low development expenses underlining the peculiarity of the entire concept. Here, the boost in exciton annihilation rates is accompanied by a set of additional pivotal benefits.

For the case of the laterally extended QWs, the exciton decay rate does not necessarily limit the quantum efficiency but still governs the ultimate operation speed rendering the light emission from polar QWs a rather slow phenomenon with limited light-emission density. For example, an electrical carrier injection into the matrix material surrounding the QW(s) leads to an exciton population that decays with a polarization-limited rate, while the device's emission intensity relies on pump power in combination with a certain lateral size of the QW. Here, the main advantage of the IFGARD concept is the miniaturization of lateral dimensions and the opportunity to further increase the pump power due to the enhanced device speed (no saturation), e.g., in VCSEL (vertical-cavity surface-emitting-laser) arrays, in addition to the aforementioned spectral narrowing of the emission. However, in the regime of high carrier-injection levels, an alternative effect of charge carriers screening the built-in polarization fields of heterostructures can be observed, which partially enables high external quantum efficiencies exceeding 50%, e.g., in (In, Ga)N/GaN LED structures [21], in an indirect way. In contrast, as soon as smaller nanostructures, e.g., like zero-dimensional QDs, are considered, a low exciton annihilation rate spoils the monochromatic emission, as each QD must not be populated by more than one exciton forbidding high carrier-injection levels that will otherwise allow for a field screening. The so-called ground-state exciton has to decay with a rate that surpasses the QD fill rate. Otherwise, the formation of multiexcitons with deviating emission energies occurs [17]. In this context, the IFGARD-enhanced recombination rate of the ground-state exciton indirectly suppresses parasitic channels, which boosts the quantum efficiency. Therefore, charge carriers should remain in the matrix material for a time frame governed by the exciton lifetime, which, however, enables a strong influence of parasitic decay channels. Hence, the IFGARD concept is of utmost value as soon as polar QDs [22–26] [e.g., [0001]-wurtzite GaN, ZnO, or [111]-zinc-blende (In,Ga)As QDs] are considered, as both the device speed and quantum efficiency can be raised.

Generally, the boost in exciton annihilation rates by the IFGARD originates from an improved electron and hole wave-function overlap that also reduces the electric dipole moment [27,28]. As a direct consequence, an electrostatic coupling to possible charge fluctuations of nearby defects is drastically reduced [3,29]. At the same time, a coupling to phonons diminishes [30,31] due to the reduced electron-hole separation, a most pivotal effect for electrically triggered one- and two-photon sources [26,32] operating at room temperature. Hence, the (optical) characteristics of such next-generation quantum-light sources based on the IFGARD will no longer be dominated by the QCSE as frequently reported for III-nitride nanostructures [27,28], despite the screening that is already achieved by free carriers [33]. The emission of each individual QD will not only become brighter but also more energetically defined and less temperature sensitive [33].

IFGARD LEDs and LDs directly raise the question for an electrical contact and bipolar doping. Here, it is of great advantage that the outer guard layers of the IFGARD-based structure comprise the same material as the nanostructure in the active region. Electrical contacts and the bipolar doping of, e.g., GaN, are nowadays straightforwardly realizable [1,34–36], whereas similar achievements of identical practicability are not yet accessible for AlN and result in excessive research efforts [37–39]. The electrical excitation of a single IFGARD QD is always based on a tunneling process through the thin barrier layers comprising a material with a larger band gap. Therefore, the tunneling probability is enhanced across the lateral extent of the QD and otherwise—between the QDs—reduced due to the increased barrier thickness; cf. Fig. 1(d). In this sense, the IFGARD even enables a current channeling through the individual QDs, an effect that is otherwise achieved in single-QD devices by complex processing of apertures [40]. Please note that exactly the same effect is also relevant for extended structures, e.g., like one-dimensional quantum wires.

VI. SUMMARY

In summary, we suggest a general field-guarding concept for polar semiconductor heterostructures that not only boosts the radiative exciton decay rates but even establishes the electric potential as a tunable parameter. Hence, based on our study, we expect the realization of, e.g., (quantum-) light sources based on polar heterostructures, whose optical signatures are decoupled from the detrimental effects of crystal polarization.

ACKNOWLEDGMENTS

We acknowledge support from the Deutsche Forschungsgemeinschaft (DFG, German Research Foundation) within the Collaborative Research Center "Semiconductor Nanophotonics" (CRC 787).

G. H., G. C., and A. H. are the inventors of the IFGARD. G. H. simulates all QD and S. W. all QW structures. G. C. and G. H. equally supervise the research project and wrote the entire manuscript.

APPENDIX A: LIGHT ABSORPTION IN THE GUARD LAYERS

At first glance, one apparent challenge of the IFGARD arises from the reabsorption of light in the guard layers. Regarding the QD from Fig. 2, we show that the exciton annihilation rate is increased by a factor of 100. This advantage is now partially counterbalanced by the light reabsorption in the guard layers. For example, we assume 50-nm-thick guard layers, which, even in a totally free-standing structure as known from one- and two-dimensional photonic crystals, still results in an mechanically stable nanodevice [41,42]. Hence, for typical GaN QD emission energies, around 50% of the emitted light gets reabsorbed [43] in the top guard layer—a tolerable effect if compared to an increased exciton decay rate (factor of 100) for the ideal IFGARD configuration; cf. Fig. 2(b). However, an already well-optimized LED structure with external quantum efficiencies approaching 50% cannot benefit from the IFGARD concept at first sight [see the discussion Sec. V for the challenging case of (In, Ga)N/GaN LEDs]. Nevertheless, please note that this first simplistic estimation does not account for the Fabry-Pérot interferences that occur in the guard layer(s). The optical transparency of the guard layers for the particular QD emission wavelength (λ) exhibits a modulation governed by the guard-layer thickness exhibiting optima at approximately $n\lambda/8$ ($n \in \mathrm{IN}$) [44]. However, such detailed design optimizations reside beyond the scope of this paper, as also the characteristic radiation pattern of the QDs must be taken into account. Nevertheless, the trivial statement that any guard-layer thickness on the order of the emitted wavelength enables sufficient transmission remains valid in consideration of the IFGARD benefits. Additionally, the light outcoupling along the c axis can further be enhanced if the local density of optical states is altered based on a cavity structure as commonly applied, e.g., for nanobeam lasers [41].

APPENDIX B: SIMULATION METHODS

It is the aim of this section to summarize our numerical procedure that facilitates the sophisticated 3D modeling for the particular case of QDs. Naturally, an in-principal equivalent but 1D method can trivially be applied to only two-dimensional structures like QWs, as additionally approved by a direct comparison to the numerical results of the NEXTNANO package. All calculations are based on an implementation of the eight-band-$k \cdot p$ formalism for wurtzite materials like nitrides, which is described in detail in the literature and is further extended for the QD case by considering the particle interactions within the Hartree-Fock approximation [20,22,45]. In the following, we provide a brief explanation of the entire set of complex calculations for the case of a QD as illustrated in Fig. 5.

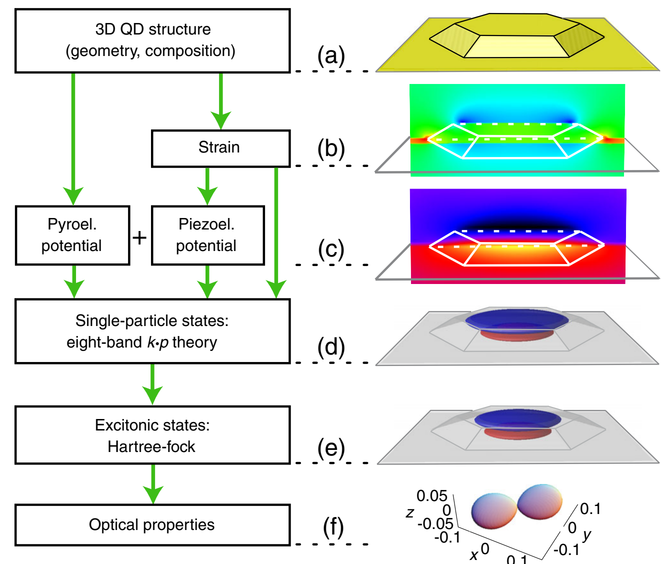

FIG. 5. Calculation scheme for the applied eight-band-$k \cdot p$ approach that yields the optical properties of the nanostructure of choice. (a) First, a nanostructure is defined before the strain distribution is continuum-mechanically calculated. The resulting ε_{zz} strain tensor component along the [0001] direction is exemplarily indicated in (b). Subsequently, the electrostatic potential (c) is derived considering the effects of pyro- and piezoelectricity of the specific crystal lattice. Solving the 8×8 Hamiltonian including the coupling of the energetically lowest conduction and the three highest valence bands (4×2 bands due to the spin projections) yields single-particle electron and hole envelope wave functions (d). An additional consideration of particle interactions (Coulomb and nonclassical exchange interaction) generates converged electron-hole densities (d). Finally, the optical properties of such a two-particle state approximation are determined, yielding, e.g., the oscillator strength of the corresponding optical transition (f).

A common simulation starts with the creation of the 3D QD structure embedded in the matrix material [Fig. 5(a)], whose size, shape, and chemical composition are specified on a finite-differences grid. All these individual properties of the particular nanostructures are extracted from atomic-force [46,47] and transmission electron microscopy [31] analyses enabling a truly realistic description of such nanostructures. For the QD calculations, we choose a mesh width of 0.1 nm in a box-shaped computation area—a value well below the actual monolayer spacing, e.g., in GaN [48], of approximately 0.26 nm. A careful convergence behavior analysis of all calculation results confirms not only the chosen mesh width but also the size of the calculation area of approximately $30 \times 30 \times 20$ nm^3 $(x \times y \times z)$ as adequate [49]. Please note that such large calculation areas are problematic for any atomistic calculations [50] but are essential in order to derive realistic (optical) properties in line with various experimental results [17,22,29].

The differing crystal lattice parameters that originate from the varying chemical composition in the calculation area create a strain distribution that is iteratively calculated using a continuum mechanical model [51,52] allowing a strain relaxation in the main growth direction known as the c axis ([0001] direction). The resultant strain tensor distribution [e.g., ε_{zz} along the [0001] direction is indicated in Fig. 5(b)] affects the local electronic situation within and around the QD directly by strain-induced energy-band deformations or shifts and indirectly by so-called piezoelectric polarizations. Subsequently, the calculation of the strain-dependent piezoelectric and the pyroelectric charge distributions inherent to the wurtzite structure [2] is performed, evoking a corresponding electrostatic potential [see Fig. 5(c)], as described by the basic Poisson equation.

Generally, the careful treatment of such electrostatic potentials is also of outstanding importance for materials that crystallize in the zinc-blende configuration—a most relevant fact, for instance, for (In, Ga)As/GaAs QDs. Recently, the [111] growth direction has been a matter of intense research efforts dedicated to (In, Ga)As/GaAs [23,24]. Here, the application of the IFGARD concept can overcome the luminosity limitations of such [111]-based arsenide QDs, bringing their most prominent advantage for quantum photonics—a vanishing excitonic fine-structure splitting—to full bloom. Exactly in such arsenide materials, the second (quadratic) order of piezoelectricity has to be taken into account [53–55], while the spontaneous pyroelectricity inherent to nitrides is absent.

As soon as the electrostatic potential is known for the entire calculation area, one can straightforwardly create the Hamiltonian matrix values for each segment of the mesh. Applying the local 8×8 Hamiltonian matrix [20,56] yields the coupling of the energetically lowest conduction band and the three topmost valence bands. Here, the electrostatic potential adds to the main diagonal of the 8×8 Hamiltonian.

Furthermore, our Hamiltonian includes the effects of the spin-orbit and crystal-field coupling, which mainly affects the energy separations between the confined ground and excited hole states in addition to the band-mixing effects. A set of material parameters [57,58] is utilized for the entire calculations as further described by Winkelnkemper *et al.* [20], whereas the sign of the piezoelectric constant e_{15} has been corrected as explained by Tomić and Vukmirović [59] in reaction to the discussion in Refs. [17,22,29,60,61]. All relevant parameters are summarized in Table I. Solving the Schrödinger equation yields single-particle electron and hole envelope wave functions [51,52,62], as depicted in Fig. 5(d)—a first but rather inadequate description of an electron-hole pair because the inherent interactions are still neglected.

A more reasonable description of such two-particle state known as an exciton is given by the mean-field Hartree-Fock particle interaction approximation [45] yielding bound electron-hole densities shown in Fig. 5(e). Here, the Coulomb- and the nonclassical exchange interactions between the electron and hole are iteratively calculated leading to a renormalization of both wave functions for each iteration step until the total excitonic energy is converged. Finally, the optical transition properties of the exciton(s) formed by the converged electron and hole wave functions are determined, as exemplified in Fig. 5(f). Previously, we have successfully applied this entire numerical procedure to a detailed analysis of polar and nonpolar QDs in perfect agreement with numerous experimental results [3,27,28,31,63]. Here, even an approximation of multiexcitons was recently derived [17,22] based on the configuration-interaction method, which yields nonseparable wave functions. Generally, QD exciton simulations require a 3D description, while QW band-edge calculations can be described sufficiently within a standard 1D approach, allowing a doubling of the simulation resolution. In summary, all our simulations describe the optical properties for the nanostructure of choice based on well-established procedures as directly approved by the experimental evidence [3,27,28,31,63]—the supreme judge for modeling approaches.

APPENDIX C: STACKING OF FIELD-GUARDED ACTIVE REGIONS

Generally, all modern LED and LD structures comprise extended layer stacks of various composition [1,64] in order to boost significant parameters as charge-carrier injection, light outcoupling, quantum efficiency, etc., all aiming towards a maximization of the most pivotal device luminosity. Hence, it is a question of special importance to clarify whether the IFGARD is *generally* compatible with such extended layer stacks without treating all optimizations

TABLE I. Compilation of GaN and AlN parameters used for the eight-band-$k \cdot p$ simulations.

Parameter	GaN	AlN	Parameter	GaN	AlN	Parameter	GaN	AlN	Parameter	GaN	AlN
a (nm)	0.3189	0.3112	e_{15} (cm^{-2})	−0.326	−0.418	Δ_{SB} (eV)	0.017	0.019	a_2 (eV)	−11.3	−11.8
c (nm)	0.5185	0.4982	e_{31} (cm^{-2})	−0.527	−0.536	$m_{e\|\|}/m_0$	0.186	0.322	D_1 (eV)	−3.7	−17.1
E_{11} (GPa)	390	396	e_{33} (cm^{-2})	0.895	1.56	$m_{e\perp}/m_0$	0.209	0.329	D_2 (eV)	4.5	7.9
E_{12} (GPa)	145	137	P_{pyro} (cm^{-2})	−0.034	−0.090	$E_{P\|\|}$ (eV)	17.292	16.927	D_3 (eV)	8.2	8.8
E_{13} (GPa)	106	108	ε_r	9.8	9.1	$E_{P\perp}$ (eV)	16.265	18.165	D_4 (eV)	−4.1	−3.9
E_{33} (GPa)	398	373	E_g (eV)	3.51	6.25	E_v (eV)	0.8	0.0	D_5 (eV)	−4.0	−3.4
E_{44} (GPa)	105	116	Δ_{CF} (eV)	0.010	−0.169	a_1 (eV)	−4.9	−3.4	D_6 (eV)	−5.5	−3.4

required for an entire device. In order to illustrate this matter, Fig. 4 shows the band-edge profiles of four different stacks of $(\mathrm{Al}_{1-x},\mathrm{Ga}_x)\mathrm{N/AlN}$ QWs. The triple-QW-stacks in Figs. 4(a) and 4(b) demonstrate the invariance of the IFGARD flat-band condition against random QW and barrier height variations, with the barrier-height variations influencing the electric potential step height between neighboring QWs. In Fig. 4(c), all QWs still consist of pure GaN, while in Fig. 4(d), the gallium content is arbitrarily reduced in favor of aluminum, demonstrating the general capability of the IFGARD concept (each AlN barrier has a thickness of 0.25 nm in order to approximate one monolayer). Here, the composition variation leads to a band-edge tilt within all QWs, which is representative for the individual gallium-to-aluminum ratio. Most intriguingly, both positive and negative band-edge inclinations can be achieved, independent of the individual QW thickness. As a result, the IFGARD enables pathways for the design of highly unconventional potential landscapes, as directly illustrated in Fig. 4(d). Suddenly, the band-edge inclination inside of the nanostructure becomes a tunable parameter that can be addressed either by the composition of the active region [QW case; see Fig. 4(d)] or by the geometric implementation of the IFGARD (QD case; see Fig. 2). Nevertheless, any particular band-edge engineering for devices with an externally applied bias remains a task for future work and goes well beyond the scope of the present paper. By realizing such larger numbers of stacked IFGARD QWs, nanowires, or QDs, the different refractive indices of the active region, the barrier, and the guard materials can even be utilized for planar mode-guiding approaches not only in, e.g., 1D [41] and 2D [42] photonic crystals, but also in basic edge-emitting lasers in order to further improve the specific light-emission characteristics of the device. Here, only a sufficient thickness of the entire IFGARD stack must be reached in order to achieve any mode guiding towards, e.g., the device's side facets (perpendicular to the c axis).

APPENDIX D: ANALYSIS OF THE TECHNICAL FEASIBILITY

The growth of the heterostructures that comprise QWs, quantum wires, or QDs along with numerous additional layers serving as Bragg reflectors, electron-blocking layers, seed layers (polarity control), etc., is a well-established procedure for many of the major semiconductor compound families. Here, it is mainly the strongly polar oxide- and nitride-based correspondents that often suffer from large inherent electric fields, as they most preferentially crystallize in the wurtzite structure. Directly related, highly sophisticated heterostructures have been developed throughout the last decades and comprise extended layer stacks featuring smooth interfaces [65]. Each of the layer thicknesses (guard layer, barrier, and QW) and, if applicable, QD geometries [33,46,66] that are assumed for our demonstration of the IFGARD in Figs. 1–3 is straightforwardly achievable based on standard growth techniques, as exemplified in the following section for the particular case of nitrides. Generally, such crystal polarization is also highly relevant in (e.g., arsenide-based) cubic crystals. Here, the occurrence of piezoelectricity leads to similar detrimental effects if, e.g., the increasingly popular [111] growth direction is considered yielding major advantages for the generation of nonclassical light based on QDs [23,25,55].

Growing IFGARD heterostructures, e.g., based on nitride material, can be achieved directly as long as all layers do not exceed the critical thickness for the plastic relaxation characteristic of the specific material system. Here, as an example, Fig. 2 assumes an AlN barrier-thickness variation from 0.5 to 2.5 nm, well above the thickness of one monolayer and beneath the critical thickness of AlN grown on GaN of approximately 3 nm [67]. Hence, as long as all layers are sufficiently thin, they are pseudomorphically strained, and, e.g., the growth of AlN on GaN is straightforwardly feasible, while the appearance of first cracks is reported for AlN thicknesses of 6–10 nm [68–71]. At the same time, the inclusion of, e.g., GaN QWs, is well possible regarding the corresponding thickness range [13,14,72] from Fig. 3, and also the growth of the matching guard layers is straightforward. Here, at least two main device categories are accessible for the IFGARD concept. First, the IFGARD stack can be grown on, e.g., a bulk GaN substrate [73] (bottom guard layer), and finally be capped by a sufficiently thin GaN layer (top guard layer) in order to ensure its optical transparency. Second, the entire IFGARD stack can be realized in a free-standing structure, e.g., like a nanobeam comprising a symmetric guard-layer configuration with thicknesses scaling up to around 100 nm, in order to achieve a sufficient mechanical stability of the final structure [41,74] along with a reasonable optical transparency (see Appendix A). We remark that the particular thickness of the guard layers provides quite a flexible option for tailoring an IFGARD-based device, as only the occurrence of the additional interfaces ensures the functionality as depicted in Fig. 3(a).

At first sight, the IFGARD favors only the inclusion of QWs as they are most preferentially, pseudomorphically strained, in contrast to QDs whose growth process itself often relies on strain relaxation. Hence, the common so-called, Stranski-Krastanov (SK) growth mode of nitride QDs [75,76] cannot straightforwardly be achieved in an IFGARD-based structure [77]. Here, the rather thin and pseudomorphically strained AlN barrier layers (see Figs. 1 and 2) do not provide a sufficient lattice mismatch for SK QDs. Nevertheless, most recent studies, e.g., on GaN QD growth, show that the underlying growth mechanism of such QDs can strongly deviate from the SK mode. A desorption-driven growth mode was reported [78] that does not rely anymore on common SK prerequisites, which is also true for the GaN QD nucleation close to structural defects [79]. Also, common droplet epitaxy [80] can generate QD growth on

pseudomorphically strained layers and is, consequently, well suited for any IFGARD QD device. Naturally, any electrical operation of the entire IFGARD structure is always based on charge-carrier tunneling through the sufficiently thin AlN barrier layers.

Tremendous efforts of the last years were dedicated to the site-controlled growth of, e.g., GaN QDs [81], enabling quantum-optical applications in the ultraviolet spectral range as described in the main article. Several techniques exist, e.g., like the QD nucleation in etch pits [82] on nanowires [32] or on strain apertures [40], which all enable positioned single QD(s) beyond the limits of a SK nucleation. In summary, all structural parameters for the active region (QWs and QDs), the barriers, and the guard layers that are assumed for a demonstration of the IFGARD concept in Figs. 1–3 are highly realistic and are not even limited to a particular nanostructure type or material system.

---

[1] B. Gil, *III-Nitride Semiconductors and their Modern Devices* (Oxford University Press, New York, 2013).

[2] O. Ambacher, J. Majewski, C. Miskys, A. Link, M. Hermann, M. Eickhoff, M. Stutzmann, F. Bernardini, V. Fiorentini, V. Tilak, B. Schaff, and L. F. Eastman, Pyroelectric properties of Al (In)GaN/GaN hetero- and quantum well structures, J. Phys. Condens. Matter **14**, 3399 (2002).

[3] C. Kindel, G. Callsen, S. Kako, T. Kawano, H. Oishi, G. Hönig, A. Schliwa, A. Hoffmann, and Y. Arakawa, Spectral diffusion in nitride quantum dots: Emission energy dependent linewidths broadening via giant built-in dipole moments, Phys. Status Solidi RRL **8**, 408 (2014).

[4] S. Kako, M. Miyamura, K. Tachibana, K. Hoshino, and Y. Arakawa, Size-dependent radiative decay time of excitons in GaN/AlN self-assembled quantum dots, Appl. Phys. Lett. **83**, 984 (2003).

[5] G. M. O. Pahn, G. Callsen, and A. Hoffmann, German Patent No. 102015217330.5 (2015).

[6] M. J. Paisley, Growth of cubic phase gallium nitride by modified molecular-beam epitaxy, J. Vac. Sci. Technol. A **7**, 701 (1989).

[7] R. M. Kemper, T. Schupp, M. Häberlen, T. Niendorf, H.-J. Maier, A. Dempewolf, F. Bertram, J. Christen, R. Kirste, A. Hoffmann, J. Lindner, and D. J. As, Anti-phase domains in cubic GaN, J. Appl. Phys. **110**, 123512 (2011).

[8] M. Bürger, G. Callsen, T. Kure, A. Hoffmann, A. Pawlis, D. Reuter, and D. J. As, Lasing properties of non-polar GaN quantum dots in cubic aluminum nitride microdisk cavities, Appl. Phys. Lett. **103**, 021107 (2013).

[9] S. Kako, M. Holmes, S. Sergent, M. Bürger, D. J. As, and Y. Arakawa, Single-photon emission from cubic GaN quantum dots, Appl. Phys. Lett. **104**, 011101 (2014).

[10] T. Paskova, *Nitrides with Nonpolar Surfaces: Growth, Properties, and Devices* (Wiley, New York, 2008).

[11] Y. Jiang, Y. Li, Y. Li, Z. Deng, T. Lu, Z. Ma, P. Zuo, L. Dai, L. Wang, H. Jia, W. Wang, J. Zhou, W. Liu, and H. Chen, Realization of high-luminous-efficiency InGaN light-emitting diodes in the "green gap" range, Sci. Rep. **5**, 10883 (2015).

[12] J. Han and M. Kneissl, Non-polar and semipolar nitride semiconductors, Semicond. Sci. Technol. **27**, 020301 (2012).

[13] M. Leroux, N. Grandjean, M. Laügt, J. Massies, B. Gil, P. Lefebvre, and P. Bigenwald, Quantum confined Stark effect due to built-in internal polarization fields in (Al, Ga)N/GaN quantum wells, Phys. Rev. B **58**, R13371 (1998).

[14] N. Grandjean, B. Damilano, S. Dalmasso, M. Leroux, M. Laügt, and J. Massies, Built-in electric-field effects in wurtzite AlGaN/GaN quantum wells, J. Appl. Phys. **86**, 3714 (1999).

[15] T. Nakaoka, S. Kako, and Y. Arakawa, Quantum confined Stark effect in single self-assembled GaN/AlN quantum dots, Physica (Amsterdam) **32E**, 148 (2006).

[16] T. Nakaoka, S. Kako, and Y. Arakawa, Unconventional quantum-confined Stark effect in a single GaN quantum dot, Phys. Rev. B **73**, 121305 (2006).

[17] G. Hönig, G. Callsen, A. Schliwa, S. Kalinowski, C. Kindel, S. Kako, Y. Arakawa, D. Bimberg, and A. Hoffmann, Manifestation of unconventional biexciton states in quantum dots, Nat. Commun. **5**, 5721 (2014).

[18] A. D. Andreev and E. P. O'Reilly, Optical transitions and radiative lifetime in GaN/AlN self-organized quantum dots, Appl. Phys. Lett. **79**, 521 (2001).

[19] A. D. Andreev and E. P. O'Reilly, Theory of the electronic structure of GaN/AlN hexagonal quantum dots, Phys. Rev. B **62**, 15851 (2000).

[20] M. Winkelnkemper, A. Schliwa, and D. Bimberg, Interrelation of structural and electronic properties in InGaN/GaN quantum dots using an eight-band $k \cdot p$ model, Phys. Rev. B **74**, 155322 (2006).

[21] F. Nippert, S. Karpov, I. Pietzonka, B. Galler, A. Wilm, T. Kure, C. Nenstiel, G. Callsen, M. Straßburg, H.-J. Lugauer, and A. Hoffmann, Determination of recombination coefficients in InGaN quantum-well light-emitting diodes by small-signal time-resolved photoluminescence, Jpn. J. Appl. Phys. **55**, 05FJ01 (2016).

[22] C. Kindel, S. Kako, T. Kawano, H. Oishi, Y. Arakawa, G. Hönig, M. Winkelnkemper, A. Schliwa, A. Hoffmann, and D. Bimberg, Exciton fine-structure splitting in GaN/AlN quantum dots, Phys. Rev. B **81**, 241309 (2010).

[23] A. Schliwa, M. Winkelnkemper, A. Lochmann, E. Stock, and D. Bimberg, In (Ga)As/GaAs quantum dots grown on a (111) surface as ideal sources of entangled photon pairs, Phys. Rev. B **80**, 161307 (2009).

[24] M. A. M. Versteegh, M. E. Reimer, A. A. van den Berg, G. Juska, V. Dimastrodonato, A. Gocalinska, E. Pelucchi, and V. Zwiller, Single pairs of time-bin-entangled photons, Phys. Rev. A **92**, 033802 (2015).

[25] G. Juska, V. Dimastrodonato, L. O. Mereni, A. Gocalinska, and E. Pelucchi, Towards quantum-dot arrays of entangled photon emitters, Nat. Photonics **7**, 527 (2013).

[26] G. Callsen, A. Carmele, G. Hönig, C. Kindel, J. Brunnmeier, M. R. Wagner, E. Stock, J. S. Reparaz, A. Schliwa, S. Reitzenstein, A. Knorr, A. Hoffmann, S. Kako, and Y. Arakawa, Steering photon statistics in single quantum dots: From one- to two-photon emission, Phys. Rev. B **87**, 245314 (2013).

[27] G. Hönig, S. Rodt, G. Callsen, I. A. Ostapenko, T. Kure, A. Schliwa, C. Kindel, D. Bimberg, A. Hoffmann, S. Kako, and Y. Arakawa, Identification of electric dipole moments of excitonic complexes in nitride-based quantum dots, Phys. Rev. B **88**, 045309 (2013).

[28] G. Callsen and G. M. O. Pahn, Identifying multi-excitons in quantum dots: The subtle connection between electric dipole moments and emission linewidths, Phys. Status Solidi RRL **9**, 521 (2015).

[29] I. A. Ostapenko, G. Hönig, C. Kindel, S. Rodt, A. Strittmatter, A. Hoffmann, and D. Bimberg, Large internal dipole moment in InGaN/GaN quantum dots, Appl. Phys. Lett. **97**, 063103 (2010).

[30] I. A. Ostapenko, G. Hönig, S. Rodt, A. Schliwa, A. Hoffmann, D. Bimberg, M. R. Dachner, M. Richter, A. Knorr, S. Kako, and Y. Arakawa, Exciton acoustic-phonon coupling in single GaN/AlN quantum dots, Phys. Rev. B **85**, 081303 (2012).

[31] G. Callsen, G. M. O. Pahn, S. Kalinowski, C. Kindel, J. Settke, J. Brunnmeier, C. Nenstiel, T. Kure, F. Nippert, A. Schliwa, A. Hoffmann, T. Markurt, T. Schulz, M. Albrecht, S. Kako, M. Arita, and Y. Arakawa, Analysis of the exciton-LO-phonon coupling in single wurtzite GaN quantum dots, Phys. Rev. B **92**, 235439 (2015).

[32] M. J. Holmes, K. Choi, S. Kako, M. Arita, and Y. Arakawa, Room-temperature triggered single photon emission from a III-nitride site-controlled nanowire quantum dot, Nano Lett. **14**, 982 (2014).

[33] S. Kako, C. Santori, K. Hoshino, S. Goetzinger, Y. Yamamoto, and Y. Arakawa, A gallium-nitride single-photon source operating at 200 K, Nat. Mater. **5**, 887 (2006).

[34] B. Monemar, P. P. Paskov, G. Pozina, C. Hemmingsson, J. P. Bergman, T. Kawashima, H. Amano, I. Akasaki, T. Paskova, S. Figge, D. Hommel, and A. Usui, Evidence for Two Mg Related Acceptors in GaN, Phys. Rev. Lett. **102**, 235501 (2009).

[35] G. Callsen, M. R. Wagner, T. Kure, J. S. Reparaz, M. Bügler, J. Brunnmeier, C. Nenstiel, A. Hoffmann, M. Hoffmann, J. Tweedie, Z. Bryan, S. Aygun, R. Kirste, R. Collazo, and Z. Sitar, Optical signature of Mg-doped GaN: Transfer processes, Phys. Rev. B **86**, 075207 (2012).

[36] H. Morkoç, *Handbook of Nitride Semiconductors and Devices: Materials Properties, Physics and Growth* (Wiley, New York, 2009), Vol. 1.

[37] Y.-B. Tang, X.-H. Bo, J. Xu, Y.-L. Cao, Z.-H. Chen, H.-S. Song, C.-P. Liu, T.-F. Hung, W.-J. Zhang, H.-M. Cheng, I. Bello, S.-T. Lee, and C.-S. Lee, Tunable *p*-type conductivity and transport properties of AlN nanowires via Mg doping, ACS Nano **5**, 3591 (2011).

[38] Y. Peng, C. Xia, H. Zhang, T. Wang, S. Wei, and Y. Jia, Tunable electronic structures of *p*-type Mg doping in AlN nanosheet, J. Appl. Phys. **116**, 044306 (2014).

[39] Y. Taniyasu, M. Kasu, and T. Makimoto, An aluminium nitride light-emitting diode with a wavelength of 210 nanometres, Nature (London) **441**, 325 (2006).

[40] W. Unrau, D. Quandt, J. H. Schulze, T. Heindel, T. D. Germann, O. Hitzemann, A. Strittmatter, S. Reitzenstein, U. W. Pohl, and D. Bimberg, Electrically driven single photon source based on a site-controlled quantum dot with self-aligned current injection, Appl. Phys. Lett. **101**, 211119 (2012).

[41] N. V. Triviño, R. Butté, J.-F. Carlin, and N. Grandjean, Continuous wave blue lasing in III-nitride nanobeam cavity on silicon, Nano Lett. **15**, 1259 (2015).

[42] N. Vico Triviño, G. Rossbach, U. Dharanipathy, J. Levrat, A. Castiglia, J. F. Carlin, K. A. Atlasov, R. Butté, R. Houdré, and N. Grandjean, High quality factor two dimensional GaN photonic crystal cavity membranes grown on silicon substrate, Appl. Phys. Lett. **100**, 071103 (2012).

[43] J. F. Muth, J. H. Lee, I. K. Shmagin, R. M. Kolbas, H. C. J. Casey, B. P. Keller, U. K. Mishra, and S. P. DenBaars, Absorption coefficient, energy gap, exciton binding energy, and recombination lifetime of GaN obtained from transmission measurements, Appl. Phys. Lett. **71**, 2572 (1997).

[44] E. Chávez-Ángel, J. S. Reparaz, J. Gomis-Bresco, M. R. Wagner, J. Cuffe, B. Graczykowski, A. Shchepetov, H. Jiang, M. Prunnila, J. Ahopelto, F. Alzina, and C. M. Sotomayor Torres, Reduction of the thermal conductivity in free-standing silicon nano-membranes investigated by non-invasive Raman thermometry, APL Mater. **2**, 012113 (2014).

[45] A. Haug, *Theoretical Solid State Physics* (Pergamon Press, Oxford, 1972).

[46] C. Kindel, S. Kako, T. Kawano, H. Oishi, and Y. Arakawa, Collinear polarization of exciton/biexciton photoluminescence from single hexagonal GaN quantum dots, Jpn. J. Appl. Phys. **48**, 04C116 (2009).

[47] C. H. Kindel, Ph.D. thesis, University of Tokyo, 2010, http://id.ndl.go.jp/bib/023384433.

[48] P. Lefebvre, S. Kalliakos, T. Bretagnon, P. Valvin, T. Taliercio, B. Gil, N. Grandjean, and J. Massies, Observation and modeling of the time-dependent descreening of internal electric field in a wurtzite GaN/Al0.15Ga0.85N quantum well after high photoexcitation, Phys. Rev. B **69**, 035307 (2004).

[49] G. M. O. Hönig, Ph.D. thesis, Technische Universität Berlin, 2015, http://dx.doi.org/10.14279/depositonce-4443.

[50] J. Neugebauer and T. Hickel, Density functional theory in materials science, WIREs Comput. Mol. Sci. **3**, 438 (2013).

[51] S. F. Borg, *Matrix-Tensor Methods in Continuum Mechanics* (World Scientific, Singapore, 1963).

[52] B. Gil, *Group III Nitride Semiconductor Compounds: Physics and Applications* (Clarendon Press, Oxford, 1998).

[53] G. Bester, X. Wu, D. Vanderbilt, and A. Zunger, Importance of Second-Order Piezoelectric Effects in Zinc-Blende Semiconductors, Phys. Rev. Lett. **96**, 187602 (2006).

[54] G. Bester, A. Zunger, X. Wu, and D. Vanderbilt, Effects of linear and nonlinear piezoelectricity on the electronic properties of InAs/GaAs quantum dots, Phys. Rev. B **74**, 081305 (2006).

[55] M. Ehrhardt and T. Koprucki, *Multi-Band Effective Mass Approximations: Advanced Mathematical Models and Numerical Techniques* (Springer, New York, 2014).

[56] D. Gershoni, C. H. Henry, and G. A. Baraff, Calculating the optical properties of multidimensional heterostructures: Application to the modeling of quaternary quantum well lasers, IEEE J. Quantum Electron. **29**, 2433 (1993).

[57] P. Rinke, M. Winkelnkemper, A. Qteish, D. Bimberg, J. Neugebauer, and M. Scheffler, Consistent set of band parameters for the group-III nitrides AlN, GaN, and InN, Phys. Rev. B **77**, 075202 (2008).

[58] I. Vurgaftman and J. R. Meyer, Band parameters for nitrogen-containing semiconductors, J. Appl. Phys. **94**, 3675 (2003).

[59] S. Tomić and N. Vukmirović, Erratum: Excitonic and biexcitonic properties of single GaN quantum dots modeled by 8-band $k \cdot p$ theory and configuration-interaction method, Phys. Rev. B **86**, 159902(E) (2012).

[60] J. Pal, G. Tse, V. Haxha, M. A. Migliorato, and S. Tomić, Second-order piezoelectricity in wurtzite III-N semiconductors, Phys. Rev. B **84**, 085211 (2011).

[61] S. Schulz, D. Mourad, S. Schumacher, and G. Czycholl, Tight-binding model for the electronic and optical properties of nitride-based quantum dots, Phys. Status Solidi B **248**, 1853 (2011).

[62] G. Bastard and J. A. Brum, Electronic states in semiconductor heterostructures, IEEE J. Quantum Electron. **22**, 1625 (1986).

[63] T. Nowozin, A. Marent, G. Hönig, A. Schliwa, D. Bimberg, A. Beckel, B. Marquardt, A. Lorke, and M. Geller, Time-resolved high-temperature detection with single charge resolution of holes tunneling into many-particle quantum dot states, Phys. Rev. B **84**, 075309 (2011).

[64] B. Gil, *Physics of Wurtzite Nitrides and Oxides: Passport to Devices* (Springer, New York, 2014).

[65] G. Schmidt, M. Müller, P. Veit, F. Bertram, J. Christen, M. Glauser, J.-F. Carlin, G. Cosendey, R. Butté, and N. Grandjean, Nano-scale luminescence characterization of individual InGaN/GaN quantum wells stacked in a microcavity using scanning transmission electron microscope cathodoluminescence, Appl. Phys. Lett. **105**, 032101 (2014).

[66] S. Kako, Ph.D. thesis, University of Tokyo, 2007, http://id.ndl.go.jp/bib/000009299355/eng.

[67] A. D. Bykhovski, B. L. Gelmont, and M. S. Shur, Elastic strain relaxation in GaN–AlN–GaN semiconductor–insulator–semiconductor structures, J. Appl. Phys. **78**, 3691 (1995).

[68] A. M. Sanchez, F. J. Pacheco, S. I. Molina, J. Stemmer, J. Aderhold, and J. Graul, Critical thickness of high-temperature AlN interlayers in GaN on sapphire (0001), J. Electron. Mater. **30**, L17 (2001).

[69] T. Koyama, M. Sugawara, Y. Uchinuma, J. F. Kaeding, R. Sharma, T. Onuma, S. Nakamura, and S. F. Chichibu, Strain-relaxation in NH 3-source molecular beam epitaxy of AlN epilayers on GaN epitaxial templates, Phys. Status Solidi (a) **203**, 1603 (2006).

[70] Y. Cao and D. Jena, High-mobility window for two-dimensional electron gases at ultrathin AlN/GaN heterojunctions, Appl. Phys. Lett. **90**, 182112 (2007).

[71] G. P. Dimitrakopulos, P. Komninou, T. Kehagias, S. L. Sahonta, J. Kioseoglou, N. Vouroutzis, I. Hausler, W. Neumann, E. Iliopoulos, A. Georgakilas, and T. Karakostas, Strain relaxation in A1NGaN heterostructures grown by molecular beam epitaxy, Phys. Status Solidi (a) **205**, 2569 (2008).

[72] P. Lefebvre, A. Morel, M. Gallart, T. Taliercio, J. Allègre, B. Gil, H. Mathieu, B. Damilano, N. Grandjean, and J. Massies, High internal electric field in a graded-width InGaN/GaN quantum well: Accurate determination by time-resolved photoluminescence spectroscopy, Appl. Phys. Lett. **78**, 1252 (2001).

[73] T. Hashimoto, F. Wu, J. S. Speck, and S. Nakamura, A GaN bulk crystal with improved structural quality grown by the ammonothermal method, Nat. Mater. **6**, 568 (2007).

[74] S. Sergent, M. Arita, S. Kako, S. Iwamoto, and Y. Arakawa, High-Q (>5000) AlN nanobeam photonic crystal cavity embedding GaN quantum dots, Appl. Phys. Lett. **100**, 121103 (2012).

[75] B. Daudin, F. Widmann, G. Feuillet, Y. Samson, M. Arlery, and J. L. Rouviere, Stranski-Krastanov growth mode during the molecular beam epitaxy of highly strained GaN, Phys. Rev. B **56**, R7069 (1997).

[76] M. Miyamura, K. Tachibana, and Y. Arakawa, High-density and size-controlled GaN self-assembled quantum dots grown by metalorganic chemical vapor deposition, Appl. Phys. Lett. **80**, 3937 (2002).

[77] D. Simeonov, E. Feltin, F. Demangeot, C. Pinquier, J. F. Carlin, R. Butté, J. Frandon, and N. Grandjean, Strain relaxation of AlN epilayers for Stranski-Krastanov GaN/AlN quantum dots grown by metal organic vapor phase epitaxy, J. Cryst. Growth **299**, 254 (2007).

[78] K. Bellmann, F. Tabataba-Vakili, T. Wernicke, A. Strittmatter, G. Callsen, A. Hoffmann, and M. Kneissl, Desorption induced GaN quantum dots on (0001) AlN by MOVPE, Phys. Status Solidi RRL **9**, 526 (2015).

[79] G. Schmidt, C. Berger, P. Veit, S. Metzner, F. Bertram, J. Bläsing, A. Dadgar, A. Strittmatter, J. Christen, G. Callsen, S. Kalinowski, and A. Hoffmann, Direct evidence of single quantum dot emission from GaN islands formed at threading dislocations using nanoscale cathodoluminescence: A source of single photons in the ultraviolet, Appl. Phys. Lett. **106**, 252101 (2015).

[80] K. Kawasaki, D. Yamazaki, A. Kinoshita, H. Hirayama, K. Tsutsui, and Y. Aoyagi, GaN quantum-dot formation by self-assembling droplet epitaxy and application to single-electron transistors, Appl. Phys. Lett. **79**, 2243 (2001).

[81] M. Holmes, S. Kako, K. Choi, P. Podemski, M. Arita, and Y. Arakawa, Measurement of an Exciton Rabi Rotation in a Single GaN/Al(x)Ga$(1-x)$N Nanowire-Quantum Dot Using Photoluminescence Spectroscopy: Evidence for Coherent Control, Phys. Rev. Lett. **111**, 057401 (2013).

[82] C. D. Yerino, P. J. Simmonds, B. Liang, D. Jung, C. Schneider, S. Unsleber, M. Vo, D. L. Huffaker, S. Höfling, M. Kamp, and M. L. Lee, Strain-driven growth of GaAs (111) quantum dots with low fine structure splitting, Appl. Phys. Lett. **105**, 251901 (2014).